Integration of Sentinel-1 and ALOS/PALSAR-2 SAR datasets for mapping active landslides along the Jinsha River corridor, China

Xiaojie Liu [a], Chaoying Zhao [a,*], Qin Zhang [a], Zhong Lu [b], Zhenhong Li [a,c], Chengsheng Yang [a], Wu Zhu [a], Jing Liu-Zeng [d], Liquan Chen [a], Chuanjin Liu [e]

[a] School of Geological Engineering and Geomatics, Chang'an University, Xi'an, Shaanxi, China
[b] Roy M. Huffington Department of Earth Sciences, Southern Methodist University, Dallas, USA
[c] COMET, School of Engineering, Newcastle University, Newcastle upon Tyne NE1 7RU, UK
[d] Institute of Surface-Earth System Science, Tianjin University, Tianjin, China
[e] The Second Monitoring and Application Center, China Earthquake Administration, Xi'an, Shaanxi, China

ARTICLE INFO

ABSTRACT

Landslide hazards along the Jinsha River corridor pose serious threats to the lives and property of local residents and can affect the safety of hydropower facilities because of the large size, number, strong activity, and disaster chain characteristics that occur following such events (such as a landslide creating a dammed lake which fails and leads to flooding), thus attracting widespread attention in both China and the rest of the world. As there is currently no complete landslide inventory map that covers the entire Jinsha River corridor, in this study the Sentinel-1 and ALOS/PALSAR-2 datasets were employed to detect and map active landslides along the entire Jinsha River corridor. Complex geomorphological conditions, such as the humid climate, dense vegetation, and steep terrain, pose great challenges to conventional InSAR-based landslide mapping methods, which can lead to a high probability of mis-judgements and omissions of landslides. Therefore, we propose a new InSAR-based procedure that can be used to conduct large-area landslide mapping through the integration of surface deformation and geomorphological features. More than 360 SAR images covering the Jinsha River corridor were processed and more than 900 active landslides were detected and mapped over the entire Jinsha River corridor for the first time. In particular, several large-scale landslides with a length and/or width of >1 km were found. Our results show that the landslides over the Jinsha River corridor are mainly located in three high earthquake-prone areas and reservoir areas, and that the landslides are mainly distributed at elevations of 1500–2000 m a.s.l. and have slope angles of 15–25°. Moreover, the deformation time series results indicate that the heavy rainfall in the summer and the rapid decline of water level in the Jinsha River might be two significant factors that accelerate the deformation of active landslides and reactivate unstable slopes. The findings in this research can be directly applied to landslide hazard mitigation and prevention along the entire Jinsha River corridor. In particular, the proposed procedure can be used for the efficient and systematic mapping of active landslides in other regions with similarly complex geomorphological conditions.

1. Introduction

As the upper reaches of the Yangtze River, the Jinsha River is internationally known for its abundant hydropower resources, which are closely related to the high gradient of the river and the topographic relief within the catchment. The river flows through an area of steep topography as a result of the strong crustal movement and frequent seismic activities that occur in the Jinsha River catchment (Li et al., 2006; Liu et al., 2011; Hu et al., 2020). These complex geological and geomorphological conditions, combined with high annual precipitation, contribute to the extensive distribution and strong activities of geohazards, including landslides, rockfalls, and debris flows (Xu et al., 2013). As a consequence, the narrow and deeply incised Jinsha River has undergone obstruction due to the mass movement of deposits many times in the past (Li et al., 2006). The most recent landslides occurred on October 11 and November 3, 2018, when two successive landslide events reached Jinsha River near Baige village at the border between Tibet and Sichuan Province in China, generating a barrier lake and

* Corresponding author.
  E-mail address: cyzhao@chd.edu.cn (C. Zhao).

blocking the river for several days (Liang et al., 2019). The chain of disasters that was caused by these two successive landslide events led to significant economic loss (Liu et al., 2020). As a result, landslide hazards in the Jinsha River corridor have once again attracted widespread attention. Many studies have been conducted analyzing the distribution characteristics, failure mechanisms, and stability issues that are associated with landslides in this area (Zhang et al., 2011; Iqbal et al., 2018; Zhao et al., 2018; Song et al., 2018). However, previous studies have mainly focused on small and targeted areas due to the limitations of the available techniques and the complex geomorphological conditions in the Jinsha River valley. As a result, the systematic mapping and investigation of the distribution characteristics, deformation patterns, and causative factors of landslide hazards is lacking for the entire Jinsha River corridor.

It is therefore critical that an accurate and up-to-date landslide inventory map is generated in order to mitigate and prevent such hazards, and particularly for the investigation of landslide susceptibility (Harp et al., 2011; Du et al., 2020). Many approaches can be used to create a landslide inventory map. The traditional method is field geological surveys; however, this is no longer economically viable for widespread areas (Wasowski and Bovenga, 2015). Optical remote sensing allows the rapid detection and mapping of landslides over wide areas through the visual interpretation of surface geomorphological features such as scarps, double ridges, bulging toes, and trenches (Zhuang et al., 2018). For example, Behling et al. (2016) used multi-sensor optical remote sensing images to derive multi-temporal landslide inventory maps in southern Kyrgyzstan. Optical remote sensing can delineate the boundary and the area affected by landslides (Rosi et al., 2018). However, it is difficult to assess the stability and susceptibility of the landslide using this method. Moreover, this approach is susceptible to external factors such as the subjective opinions of experts, leading to the possibility of false negatives (FN) or false positives (FP) in terms of landslide detection and mapping.

SAR interferometry (InSAR) is one of the most advanced tools for detecting and mapping landslides and can cover areas with a broad range of climatic, geomorphic, and vegetation conditions (Zhao et al., 2012; Wasowski and Bovenga, 2015; Nishiguchi et al., 2017). The InSAR method uses differences in the phase measurements to map the deformation of the earth's surface, and can therefore contribute to generating landslide inventory maps according to these features (e.g., annual deformation rate) (Scaioni et al., 2014; Wasowski and Bovenga, 2014; Dong et al., 2018), while reaping the advantages of a wide spatial coverage and the capability for constant operation in all weather conditions. The benefits of using InSAR for landslide mapping are threefold: the detection of previously unknown active slopes, the accurate delineation of boundaries that surround active slopes, and the assessment of landslide activity (Scaioni et al., 2014).

However, several challenges and shortcomings remain when using InSAR technology to detect and map landslides owing to geometrical distortions, temporal and volume decorrelation, and severe atmosphere artifacts in areas characterized by a humid climate, dense vegetation, and steep terrain (Wasowski and Bovenga, 2014). As a result, previous InSAR-based landslide investigations of the Jinsha River corridor were concentrated in small areas that have good observation conditions. For instance, Zhao et al. (2018) employed ALOS/PALSAR-1 images to detect and monitor potential landslides in the Wudongde reservoir area (2500 km^2) of the Jinsha River corridor. Moreover, the deformation rate has often been used as the only indicator for detecting and mapping active landslides in previous studies (Shi et al., 2016; Dong et al., 2018; Zhao et al., 2018; Shi et al., 2019), which has worked well under good observation conditions. However, there may be a possibility of misjudgement and omissions when detecting landslides in the Jinsha River corridor if only the deformation rate is considered. Additionally, most of the cases in which InSAR has been applied to landslide investigation in China have been concentrated to a relatively small scale of less than 10,000 km^2 (Wang et al., 2013; Zhang et al., 2015; Shi et al.,

2016; Zhao et al., 2018; Liu et al., 2018; Shi et al., 2019). Few studies have focused on investigating catchment scale landslides that reach lengths of 2000 km using the InSAR method.

In this study, multi-source SAR images and multi-temporal optical remote sensing images were integrated to detect and map active landslides over the entire Jinsha River corridor. A total of 364 SAR images acquired by the C-band Sentinel-1 and L-band ALOS/PALSAR-2 sensors were collected and processed using an automated/semi-automated data processing procedure. Errors related to phase unwrapping, the digital elevation model (DEM), and atmospheric delay were carefully checked for and corrected to generate accurate surface deformation maps and a new InSAR-based procedure was developed to detect and map active landslides in geomorphologically complex areas by integrating the surface deformation features with the geomorphological features. The InSAR-based procedure developed in this study not only improves the accuracy and reliability of landslide detection but also overcomes the shortcomings of large-area active landslide mapping that is carried out using a single type of information. Furthermore, the time series deformation of several specific slopes was analyzed against monthly precipitation and the variation in the water level of Jinsha River, the results of which are beneficial for landslide prevention and early warning.

2. Study area

The Jinsha River (see Fig. 1a) originates in the Tanggula Mountains (5054 m a.s.l), Yushu, in the Qinghai province of China, and flows for approximately 2360 km before flowing into the Yangtze River at Yibin, Sichuan province (253 m a.s.l) (Li et al., 2006; Zhou et al., 2010). The river flows through four provinces: Qinghai, Sichuan, Tibet, and Yunnan in western China, and can be divided into three sections (see Fig. 1a): the upper reaches from Yushu to Shigu in Yunan province that covers a length of 994 km; the middle reaches from Shigu to Panzhihua, Sichuan province with a length of 564 km; and the lower reaches that cover the river from Panzhihua to Yibin, with a length of 733 km (Liu et al., 2011). The Jinsha River is characterized by deeply incised valleys and relatively high gradients in the river profile, rendering it ideal for the construction of large hydropower projects. To date, 23 hydropower stations have been designed and are expected to be built on Jinsha River.

Jinsha River lies at the transition zone that is sandwiched between the Qinghai–Tibet Plateau, Yunnan–Guizhou Plateau, and Sichuan Basin in China, generating a particularly complex geological setting (Li et al., 2006; Liu et al., 2011). Fig. 1b shows the geology along the Jinsha River corridor at a scale of 1:2500000, from which it is apparent that the strata are comparatively integrated and include Carboniferous (*C*), Jurassic (*J*), Triassic (*P*), and Silurian (*S*) strata. The Carboniferous strata comprise limestone, conglomerate, slate, and quartz sandstone, which are easily weathered, producing layers in which the shearing strength decreases after infiltration by rainfall. The Silurian strata consist of mudstone, carbonaceous shale, coal, shale, and powdery sandstone and include crannies that can hold water, which is detrimental to the stability of the slopes (Li et al., 2006). The Jurassic strata are composed of feldspar–quartz sandstone, sandy mudstones, and amaranthine mudstones, which are thin and prone to failure under the effects of gravity and rainfall (Li et al., 2006).

The tectonic movement in the Jinsha River corridor is extremely strong, with an annual horizontal deformation rate reaching as high as 18–32 mm/year from 1998 to 2018 (Yu et al., 2019). A total of 44 faults pass through the study area (denoted by red lines in Fig. 1b), of which 14 are currently active. Several strong earthquakes have occurred in these active fault zones in the past, such as the Mw. 7.1 Yushu earthquake that occurred in the Ganzi–Yushu fault zone in 2010 and the strong Batang earthquake group with a Mw. > 6.2 that occurred in the Jinsha River fault zone in 1989.

The complex geological structure, strong crustal movements, frequent seismic events, and human activities contribute to the extensive distribution and extraordinary activity of the landslide hazards that
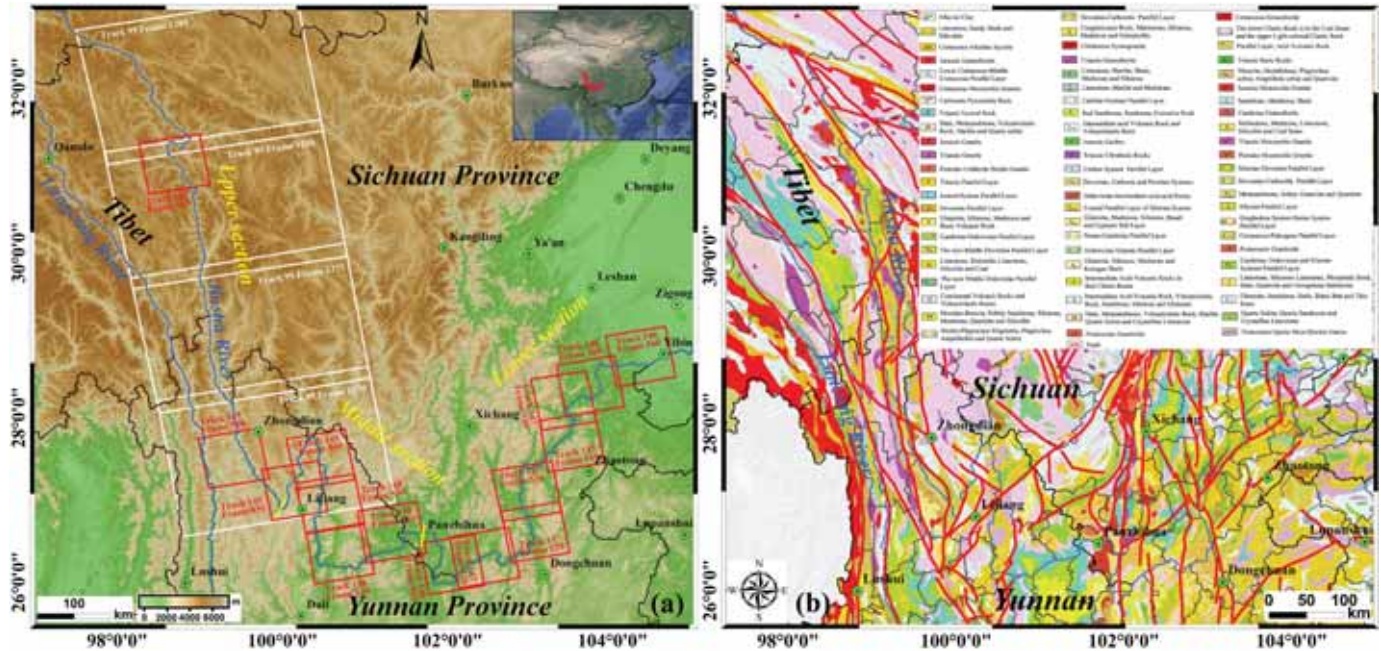
Fig. 1. (a) Location of the Jinsha River and coverage of the SAR datasets. White rectangles indicate the coverage of the Sentinel-1 dataset, whilst the red rectangles show the ALOS/PALSAR-2 images. The green solid circles describe the locations of the main cities. (b) The geology along the Jinsha River corridor collected from the Geological Cloud, China Geological Survey (http://geocloud.cgs.gov.cn/#/portal/home). (For interpretation of the references to colour in this figure legend, the reader is referred to the web version of this article.)

Fig. 2. The case of the Baige landslide, Jinsha River (source: https://image.baidu.com/). (a) View after the occurrence of the landslide on October 11, 2018; (b) road damage; (c) flooded houses; and (d) bridge damage.

occur in the Jinsha River corridor (Iqbal et al., 2018). In addition, landslide destabilization or failure during reservoir impoundment poses serious threats to the safety and normal operation of hydropower stations. Fig. 2 shows four field photos that were taken after the occurrence of the Baige landslide on October 11, 2018 (see Fig. 2a). The images indicate that after the landslide occurred and blocked the Jinsha River, a chain of disasters followed, causing damage in the lower reaches of the landslide that included the demolition of buildings (see Fig. 2c) and transportation facilities (see Figs. 2b and d).

3. Data and methodology

3.1. Data

The Jinsha River, which is in a mountainous area in western China, was selected as the study area. The vegetation is relatively sparse in the dry-hot valley section that characterizes the upper reaches of the river, whereas it is very dense in the middle and lower reaches. Accordingly, SAR images using two different wavelengths; C-band Sentinel-1 and L-band ALOS/PALSAR-2, were employed to avoid omissions and misjudgments that often occur when detecting landslides that result from temporal and/or volume decorrelation (Kang et al., 2017). A total of 193 Sentinel-1 images were acquired from 4 frames on an ascending track (i. e., Track 99 Frames 1270, 1275, 1280, and 1285) during the period from March 18, 2017 to November 20, 2018, and 171 ALOS/PALSAR-2 images were acquired from 15 frames on 4 ascending tracks (Track 146 Frame 560; Track 147 Frames 520, 530, 540, and 550; Track 148 Frames 510, 520, 530, and 540; and Track 149 Frames 530, 540, and 610) covering the period from September 17, 2014, to March 27, 2019. The spatial coverage of each SAR dataset is shown in Fig. 1a, and the time period covered for each SAR dataset is presented in Table S1. Two different types of DEMs, a one arc-second SRTM DEM and an AW3D30 DSM, were employed to generate the topographic factors and remove the topographic phase components.

To extract the surface geomorphological features, multi-temporal optical remote sensing images (see Table S2 for details) covering the entire Jinsha River corridor were sourced from the Sentinel-2 satellite and the Google Earth platform at spatial resolutions between 0.3 and 16 m. The historical earthquakes that occurred between 1216 and 2019 were used to analyze the impact of seismic activity on the distribution of landslides. The monthly precipitation between February 1, 2017, and December 1, 2018, from the Global Precipitation Measurement (GPM)

(Huffman et al., 2019) and the Jinsha River water level variations at the Xiluodu reservoir between December 12, 2014 and July 2, 2017 (Chen and Dai, 2018) were collected to investigate the primary causative factors of landslides so as to facilitate the understanding of the landslide deformation mechanisms.

3.2. Methodology

Most of the study area is characterized by a humid climate, flourishing vegetation, and steep topography, which makes it challenging to detect landslides using SAR interferometry. Steep topography often leads to the geometrical distortion of SAR images (Liu et al., 2018), and a humid climate and flourishing vegetation can lead to problems with volume and/or temporal decorrelation (Kang et al., 2017). These factors often lead to considerable uncertainties in the measurement of
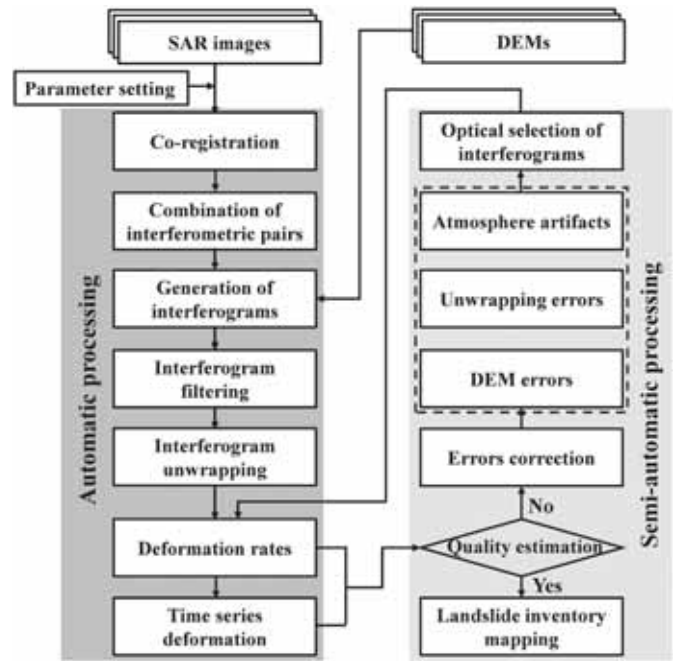

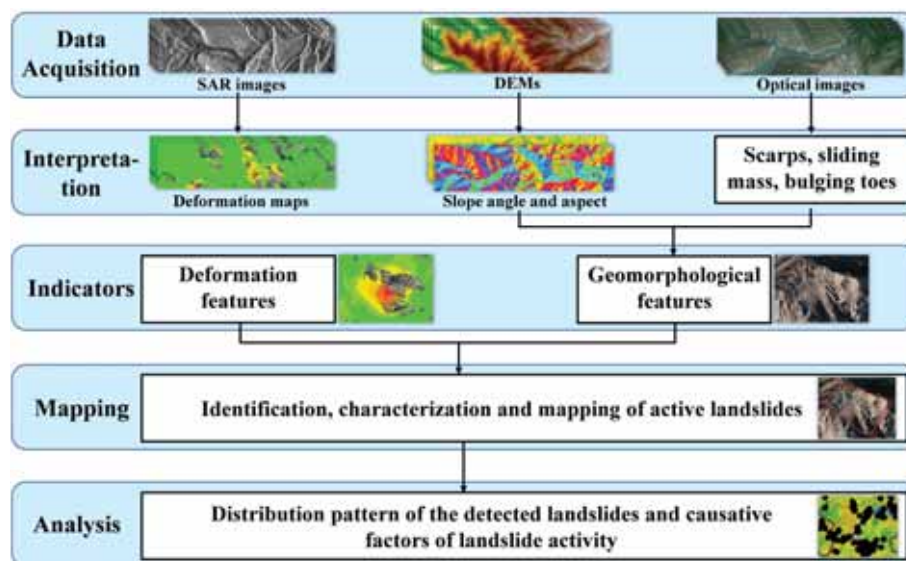**Fig. 4.** Workflow used for InSAR processing.

Fig. 3. Flowchart of the methodology adopted for mapping and characterization of landslides that cover large areas.

deformation, leading to a high probability of mis-judgement and omissions in landslide detection and mapping. Therefore, we propose a new InSAR-based procedure for large-area active landslide mapping in geomorphologically complex areas with a steep topography, dense vegetation cover, and humid climate, as shown in Fig. 3.

First, multi-source SAR images, DEMs, and multi-temporal optical remote sensing images were acquired and processed. An automated/semi-automated SAR data processing strategy (see Fig. 4) was employed to generate annual deformation rates and time series deformation maps, and the Sentinel-2 images were processed using the European Space Agency (ESA) SentiNel Application Platform (Veci et al., 2014). DEMs were used to generate topographic derivatives, including slope angle and aspect. Multi-temporal optical remote sensing images were employed to extract geomorphic features such as scarps, sliding masses, and bulging toes.

The annual deformation rates, time series deformation maps, and topographic factors were then matched with an identical geographic grid under the same coordinate system. The preliminary detection and mapping of suspected active landslides were carried out through integrating the annual deformation rate maps, time series deformation maps, and topographic factors. It is worth mentioning that the annual deformation rate maps were used to detect slow-moving landslides, while the time series deformation maps were used to detect landslides with oscillating deformation patterns (such as step-like landslides with a zero mean deformation rate (Zhou et al., 2018)). An annual deformation rate of 1 cm and a slope angle of 5° were set as thresholds for the detection and mapping of possible active landslides. A slope was considered as a suspicious active landslide when the annual deformation rate was less than −1 cm or greater than 1 cm and the slope angle was greater than 5°. The slope aspect was used to determine whether the direction in which the landslide moved was correct, so that any errors resulting from local residual atmospheric artifacts could be excluded.

The suspicious active landslides were then superimposed onto the multi-temporal optical remote sensing images and were further screened according to the surface geomorphological features (e.g., scarps, sliding masses, and bulging toes) to any eliminate misjudged landslides and to finalize the landslide mapping. It is worth noting that the spatiotemporal deformation characteristics were further used to ascertain whether a landslide was active in some regions with obvious deformation but no clear geomorphological features on the remote sensing images. Taking the Ludila reservoir area as an example, the detailed procedure and immediate results for every step of landslide detection and mapping are presented in Fig. S5.

Finally, we generated an inventory map of the active landslides detected, including the location, size, boundary, and deformation magnitude of the landslides. The distribution pattern of the detected landslides with respect to topographic factors was also analyzed, and the primary causative factors for landslide activity were investigated via the correlation between the time series landslide deformation, monthly precipitation, and the variation in the Jinsha River water levels.

3.2.1. InSAR processing

The automated/semi-automated data processing procedure presented in Fig. 4 was used to process the SAR images in order to efficiently and quickly handle the substantial amount of SAR data involved. First, all SAR images and ancillary data (e.g., precise orbit files) covering the whole study area were downloaded and preprocessed. Then, on the basis of previously defined parameters, all possible interferograms were automatically generated, filtered using an adaptive filtering function based on the local fringe spectrum (Goldstein and Werner, 1998), and unwrapped using the minimum cost flow (MCF) algorithm (Costantini, 1998). Estimation of an initial deformation rate map using the weighted averaging of interferograms (i.e., Stacking) method was subsequently conducted (Lyons and Sandwell, 2003). This was followed by inversion of the initial time series deformation through the least square (LS) criterion or singular value decomposition (SVD) (Berardino et al., 2002).

There were directly used for landslide detection if the quality of the estimated deformation results met the requirements. If not, errors related to atmospheric artifacts, residual baseline errors, phase unwrapping errors, and DEM errors in the unwrapped interferograms, were carefully checked for and corrected. Finally, high-quality corrected unwrapped interferograms were selected to re-estimate the deformation rates and time series. The temporal and spatial baselines were set at 60 d and 250 m, respectively, to generate interferograms for the Sentinel-1 dataset. A full combination with the ALOS/PALSAR-2 dataset was performed because only a small number of SAR images were available.

Dense vegetation and heavy precipitation in a study area can lead to strong decorrelation, which increases the difficulty of phase unwrapping. Thus, the trade-offs between the multi-looking factor, filtering window size, and landslide detection capability should be well considered when processing SAR images. In this study, a multi-looking factor of 4 in range (i.e., a resolution of approximately 17 m in the ground direction) and 1 in azimuth (i.e., a resolution of approximately 14 m) were used to process the Sentinel-1 SAR images, while a factor of 2 in range (i.e., a resolution of about 13 m in the ground direction) and 4 in azimuth (i.e., a resolution of approximately 13 m) were used to process the ALOS/PALSAR-2 images. Interferograms with this resolution can detect landslides as small as 100 m in each dimension. A small window size was used to filter all the interferograms to avoid the loss of information at the edge of fringes. Phase unwrapping errors are inevitable for some interferograms with low coherence; in these cases the phase unwrapping errors were corrected using either phase compensation, which involves subtracting or adding an integer number of phase cycle (s) at the phase jump pixels, or unwrapping a phase at pixels with high coherence (Liu et al., 2018). Fig. S1 shows some unwrapped interferograms with Track 146 Frame 560 of the ALOS/PALSAR-2 data (Zone 6 marked in Fig. 5) before and after the phase unwrapping error correction. In addition, areas that include SAR geometrical distortions (i.e., layover and shadow) in the interferograms were masked to avoid misleading information.

Large-area deformation estimation is usually contaminated by tropospheric delay, which is considerably severe in areas with humid climates and steep topography. Therefore, two different approaches were employed to eliminate the InSAR tropospheric delay. In the first approach, the tropospheric delay was estimated and mitigated using the GACOS atmospheric products (Yu et al., 2018a, 2018b), while the second involved the consideration of an empirical linear model connecting the InSAR phase delay to the elevation (Doin et al., 2009). Fig. S2 shows some unwrapped interferograms from Track 99 Frame 1280 of the Sentinel-1 data, and Fig. S3 shows the results from Track 147 Frame 520 of the ALOS/PALSAR-2 data (Zone 5 marked in Fig. 5) before and after the tropospheric delay was corrected. A quadratic polynomial model was also applied to correct the residual baseline errors in the unwrapped interferograms (Liu et al., 2019). Fig. S4 exhibits some exemplary unwrapped interferograms from Track 149 Frame 610 of the ALOS/PALSAR-2 data before and after baseline error correction.

As the acquisition dates of the SRTM DEM and AW3D30 DSM were from around the year 2000 and from 2006 to 2011, respectively, the topographies in some regions in the study area have changed. Therefore, we needed to correct the DEM errors before inversion of the deformation was performed. To this end, the DEM errors were first estimated using interferograms from dry seasons with long spatial baselines and short temporal baselines assuming no deformation signals (Liu et al., 2018), which were then used to update the original DEM.

4. Results and analyses

4.1. Deformation results

Fig. 5 shows the annual deformation rate map in the line-of-sight (LOS) direction derived from the ALOS/PALSAR-2 and Sentinel-1 SAR images along the Jinsha River corridor from Yushu, Qinghai Province to
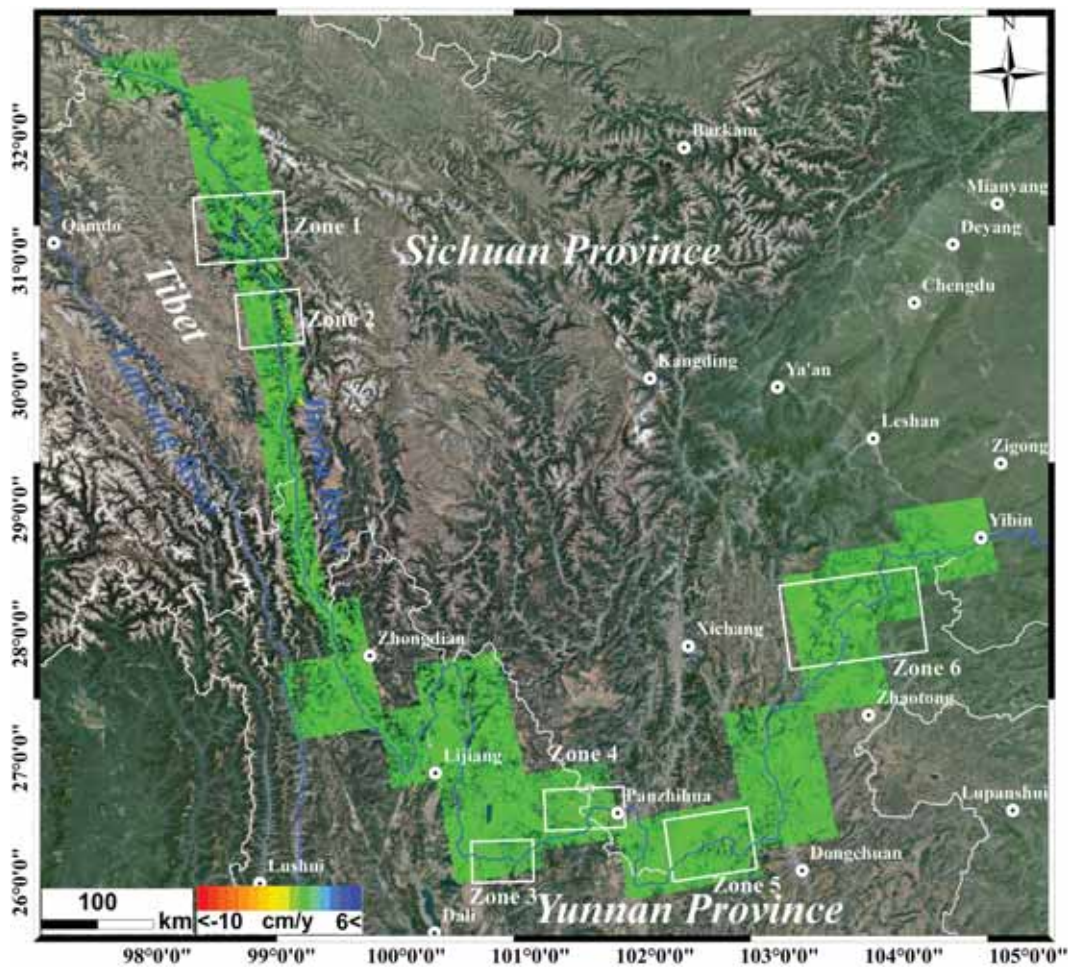
Fig. 5. Annual deformation rate map in the line-of-sight (LOS) direction along the Jinsha River corridor based on Sentinel-1 and ALOS/PALSAR-2 images.

Yibin, Sichuan province, which cover an area of approximately 81,667.6 km^2 over a length of approximately 2000 km. Positive value (blue colour) represents a landslide moving toward the sensor and negative value (red one) indicates movement away from the sensor. The map of the annual deformation rate suggests that the landslides are distributed unevenly along the Jinsha River corridor. Large-scale landslides were mainly concentrated in the six regions outlined with white rectangles in Fig. 5: the region between Jiangda county of Tibet and Dege and Baiyu counties of Sichuan province (i.e., Zone 1); Gongjue County in Tibet (i.e., Zone 2); the Ludila reservoir area (i.e., Zone 3); Jinsha and Guanyinyan reservoir areas (i.e., Zone 4); Wudongde reservoir area (i.e., Zone 5); and the Xiluodu reservoir area (i.e., Zone 6). Fig. 6 shows the enlarged maps describing the annual deformation rate for the six regions, in which many large-scale landslides with deformation rates greater than 10 cm/y in the line-of-sight (LOS) direction can be observed. In particular, six large-scale landslides with a length and/or width greater than 1 km were detected in Zone 2 (see Fig. 6b).

To evaluate the consistency of the deformation results derived from different satellites and/or tracks, Fig. 7 shows histograms of the differences in the deformation rate within the overlapped areas from independent SAR images from different satellites and/or tracks. The mean value and standard deviation of the differences between the deformation rate on common pixels in the Sentinel-1 and ALOS/PALSAR-2 images are 1.6 and 9.8 mm/y, respectively (see Fig. 7a). The disparity between the results from the Sentinel-1 and ALOS/PALSAR-2 images may be caused by three factors. First, SAR satellites with different imaging geometries can result in different flight directions and incidence angles. In the study area, the differences in incidence angle and azimuth between

Sentinel-1 and ALOS/PALSAR-2 images reach 2.4° and 2.3°, respectively. These differences have not been compensated for because it is challenging to project the LOS deformations derived from Sentinel-1 and ALOS/PALSAR-2 images in an identical but unknown slope direction (Shi et al., 2016). Second, the acquisition dates of the ALOS/PALSAR-2 and Sentinel-1 images were not synchronized. The deformation of a landslide is usually nonlinear; hence, differences in the observation time may lead to inconsistencies in estimating the deformation rate (Shi et al., 2016). Third, SAR images with different wavelengths have different sensitivities to deformation signals, with Sentinel-1 images being more sensitive to surface deformation than ALOS/PALSAR-2 images. The maximum standard deviation in the ALOS/PALSAR-2 results is 5.5 mm/y (Figs. 7b, c, and d), which is mainly due to inconsistencies in the local incidence angle and acquisition time for the different tracks of the ALOS/PALSAR-2 SAR images (Zhao et al., 2012; Liu et al., 2018).

4.2. Mapping active landslides

An active landslide inventory map for the Jinsha River corridor was generated from the deformation maps, topographic factors, and multitemporal optical remote sensing images based on the procedure described in Section 3.2. A total of 915 active landslides were detected and mapped, as shown by the dark blue dots in Fig. 8. The pink circles indicate earthquakes that occurred from 1216 to 2019, during which a total of approximately 350 earthquakes with a magnitude of > Mw. 4.0 occurred in the study area. To demonstrate the landslide mapping results, 18 typical landslides are highlighted together with the deformation rate maps (Fig. 9a) and the corresponding optical remote sensing
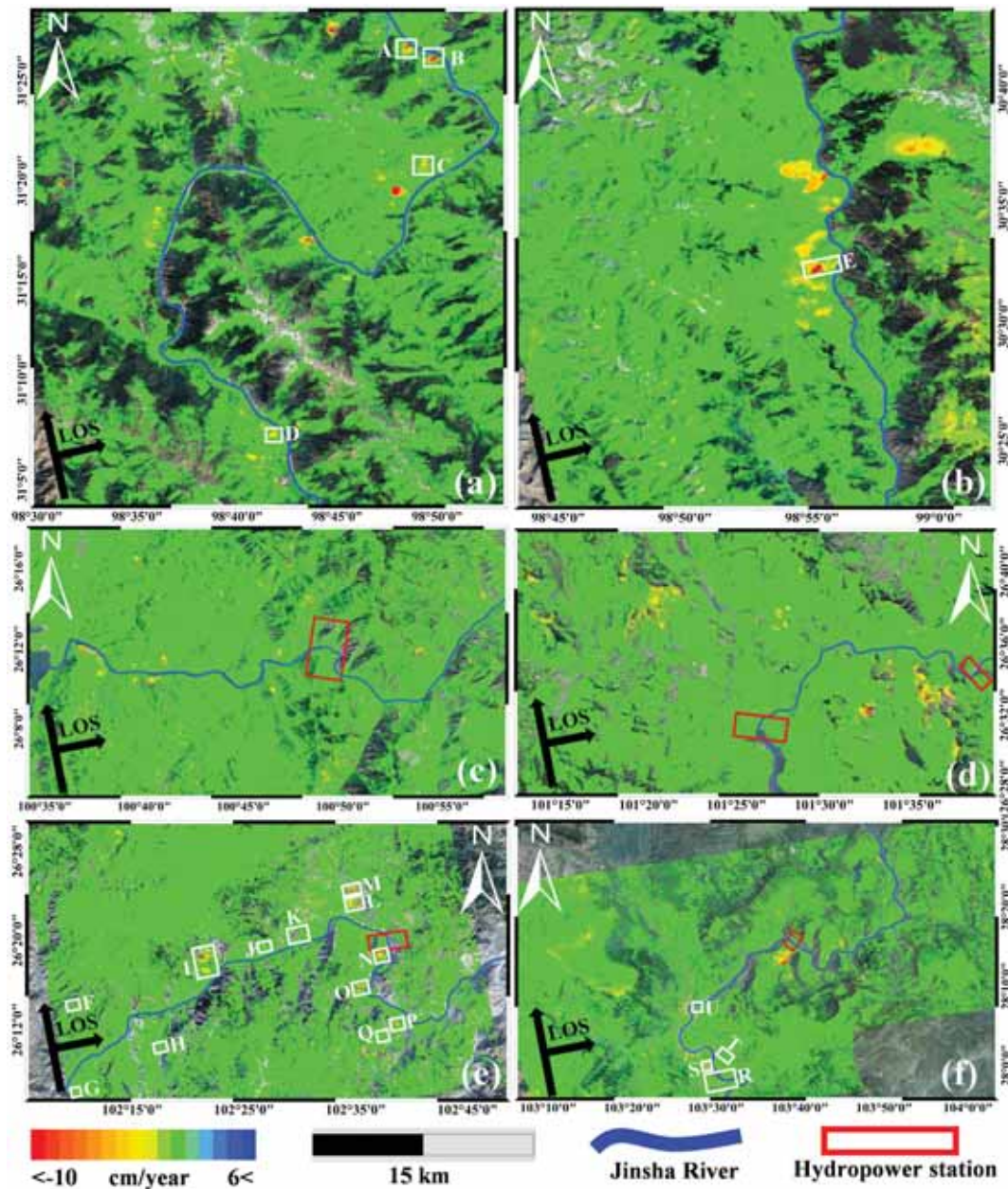
Fig. 6. Enlarged maps of annual deformation rate for six regions (marked in Fig. 5) including many large-scale landslides. The blue colour (positive value) represents a landslide moving toward the sensor and the red one (negative value) indicates movement away from the sensor. The white rectangles and corresponding letters indicate the landslides (i.e., A–E and U) that were used for the time series deformation analysis and landslides (i.e., F–T) reported in previous studies (Wang et al., 2013; Zhao et al., 2018; Li et al., 2019). (a) Zone 1; (b) Zone 2; (c) Zone 3; (d) Zone 4; (e) Zone 5; and (f) Zone 6. (For interpretation of the references to colour in this figure legend, the reader is referred to the web version of this article.)

images (Fig. 9b). As shown in these figures, the surface deformation patterns and the corresponding landslide geomorphological features match very well, and the landslide boundary derived from the deformation rate is consistent with that derived from optical remote sensing images that are based on geomorphic features. Moreover, for each landslide, the area with the largest deformation rate corresponds to the most active area on the remote sensing image. These results suggest that InSAR has significant potential for accurately delineating the boundary of a landslide and characterizing its active state. Some landslides that were detected in this study are highly consistent with those reported in previous studies, for example landslides that are in the Wudongde (Regions F–Q marked with white rectangles in Fig. 6) and the Xiluodu reservoir area (Regions R-T marked with white rectangles in Fig. 6) (Wang et al., 2013; Zhao et al., 2018; Li et al., 2019). The time series

deformations of several detected landslides are presented in Figs. S7–S12.

Fig. 8 indicates that the number of detected active landslides in the lower reaches is significantly greater than that in the upper and middle reaches of the Jinsha River, and that the active landslides are mainly concentrated around the reservoirs and in areas that are earthquake-prone. The two areas (red arrows in Fig. 8) with the highest density are near the Xiluodu (F1 in Fig. 8) and Wudongde reservoirs (F3 in Fig. 8). In addition, the number of historical earthquakes in the lower reaches is also greater than that in the upper and middle reaches. Previous studies (Liu et al., 2011) have demonstrated that the peak ground acceleration (PGA) values are higher than 0.15 g downstream of the Jinsha River. As a result, the intensities of the earthquakes in this area are generally greater than VII, and even reach IX in some areas, leading
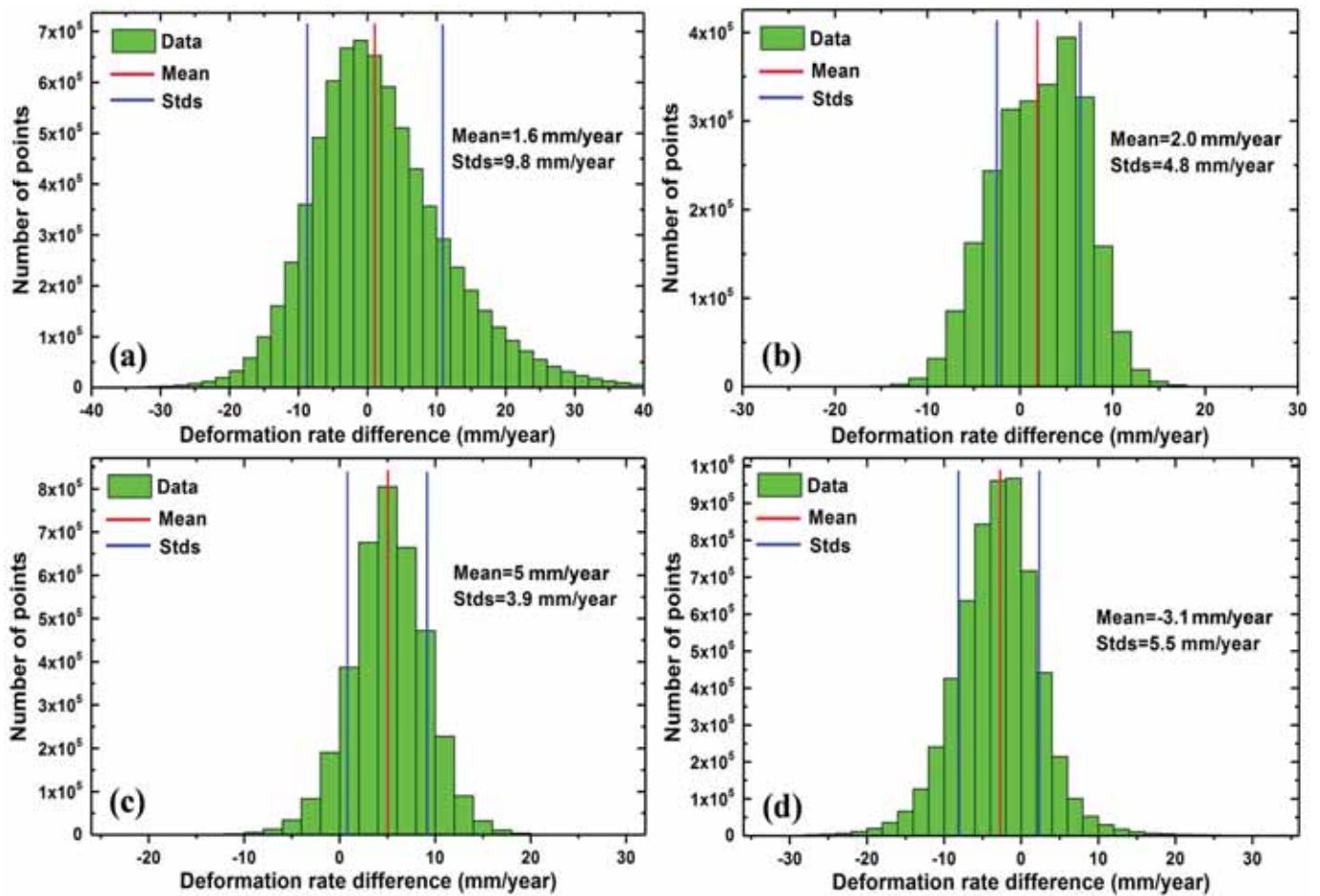
Fig. 7. Histograms of deformation rate differences within the SAR image overlap areas. (a) Between Sentinel-1 (Track 99 and Frame 1280) and ALOS/PALSAR-2 (Track 149 and Frame 610) SAR images; (b) between Track 148 (Frame 540) and Track 149 (Frame 530) of the ALOS/PALSAR-2 SAR images; (c) between Track 148 (Frame 530) and Track 149 (Frame 530) of the ALOS/PALSAR-2 SAR images; and (d) between Track 147 (Frame 520) and Track 148 (Frame 510) of the ALOS/PALSAR-2 SAR images.

to a high probability of landslide development and occurrence (Liu et al., 2011). We can also see from Fig. 8 that there are several earthquake zones located in the Wudongde and Xiluodu reservoir areas. Since 1216, approximately 15 and 42 earthquakes with $Mw. \geq 5.0$ have occurred in the area around the Wudongde and Xiluodu reservoirs, respectively. In 1974, a strong $Mw. \approx 7.1$ earthquake occurred in Yanjin, Yunnan province, which is close to Xiluodu reservoir area. In addition, dense landslides are also observed in the Baihetan reservoir area (F2 in Fig. 8), which is also prone to earthquakes (see Fig. 8). A total of 7 earthquakes with $Mw \geq 5.0$ occurred in this area from 1216 to 2019. The evidence demonstrates that the distribution of landslides in the Jinsha River corridor is significantly correlated with seismic activity.

According to previous studies (Zhang et al., 2011; Iqbal et al., 2018; Zhao et al., 2018) and the InSAR-derived deformation characteristics, we conclude that the landslides in the Jinsha River corridor are affected and triggered by multiple factors, including (1) freezing and thawing, (2) snow/glacier melt water, (3) rainfall and water level fluctuation, and (4) earthquakes. Landslides that are caused by freezing and thawing and the melting water from snow/glaciers are mainly concentrated on the upper reaches of the Jinsha River at high altitudes, while those caused by rainfall and fluctuation in the water level are mainly distributed on the lower reaches. Of the landslides detected, 69 active landslides were distributed on the left or right bank of the Jinsha River, with the relatively large annual deformation rate and volume. They may have a risk of blocking the Jinsha River and threatening the safety of hydropower stations if a failure occurs. Detailed information about these landslides is

presented in Table 1, and the spatial distribution of these landslides is shown in Fig. S6, which is expected to be useful for future monitoring.

5. Discussion

5.1. Impact factors on the results of landslide mapping

The study area covers the Jinsha River corridor, which is characterized by steep topography. Geometrical distortions including layover and shadow resulting from the side-looking acquisition mode of SAR satellites are therefore inevitable (Wasowski and Bovenga, 2014). Geometrical distortions can lead to blind areas in single-orbit observations, causing omissions in terms of landslide detection (Dong et al., 2018). To quantitatively evaluate the effects of the geometrical distortions of SAR images used in this study, we calculated the areas affected by geometrical distortion and the visibility, based on the imaging geometries (i.e., incidence angle and azimuth) of the ascending Sentinel-1 and ALOS/PALSAR-2 SAR images and the DEMs, as shown in Fig. 10. The visible area accounts for 90.2% (corresponding to 73,664 km^2) of the total study area, while the area affected by layover and shadow accounts for 9.1% (corresponding to 7431 km^2) and 0.7% (corresponding to 571 km^2), respectively. The results suggest that most of the study area has favorable conditions for landslide detection and mapping. It is worth noting that landslides located in the layover and shadow regions could not be detected in this study.

Long-wavelength ALOS/PALSAR-2 SAR images were used to
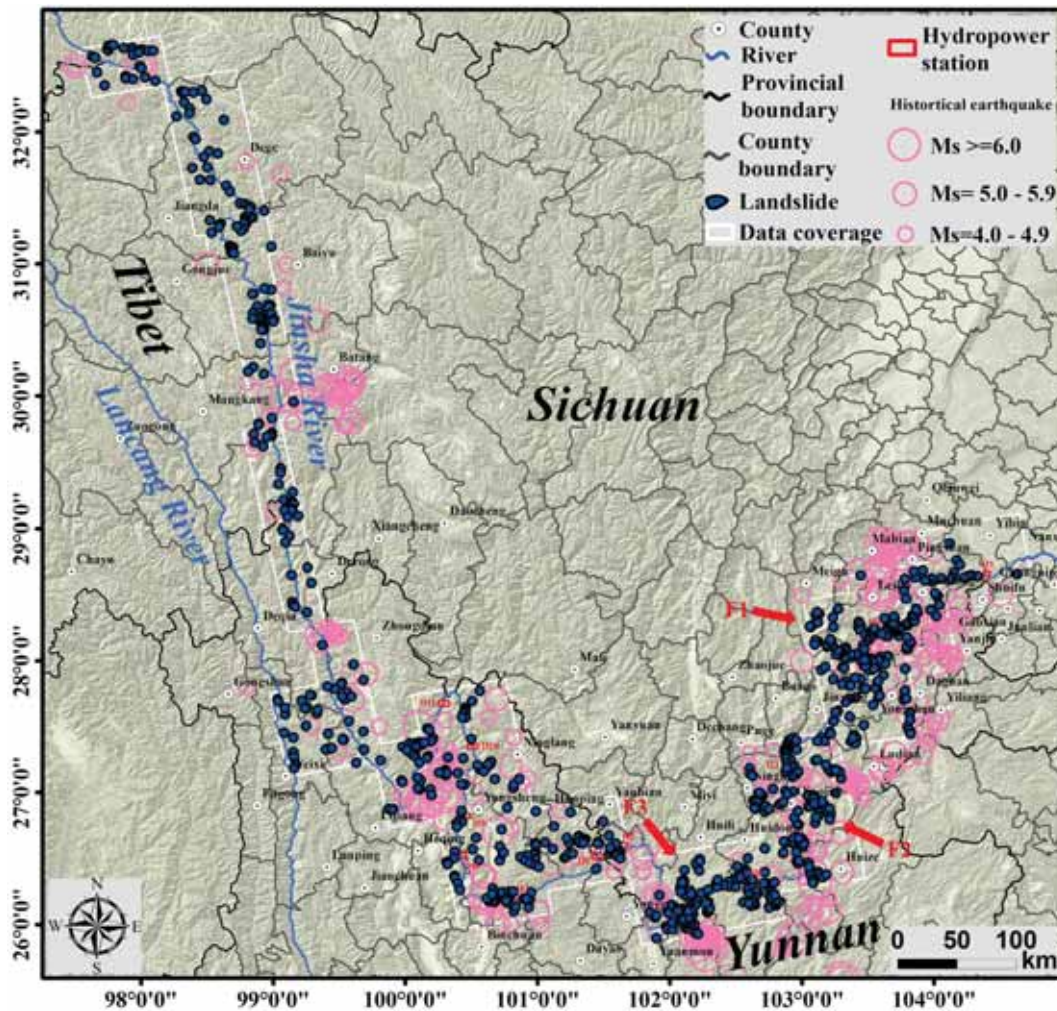
Fig. 8. Distribution of active landslides along the Jinsha River corridor detected by the ALOS/PALSAR-2 and Sentinel-1 SAR images. The dark blue dots indicate the detected active landslides, and the pink circles are the historical earthquakes that occurred from 1216 to 2019, which were collected from the China Earthquake Networks Center. H1–H11 represent the locations of the main hydropower stations (Xiangjiaba (H1), Xiluodu (H2), Baihetan (H3), Wudongde (H4), Jinsha (H5), Guanyinyan (H6), Ludila (H7), Longkaikou (H8), Jinanqiao (H9), Ahai (H10) and Liyuan (H11)), and F1–F3 are three high earthquake-prone areas. (For interpretation of the references to colour in this figure legend, the reader is referred to the web version of this article.)

minimize the effect of temporal decorrelation in areas covered with vegetation. However, some regions are still affected by temporal decorrelation due to extremely dense vegetation and large temporal baselines of the ALOS/PALSAR-2 images. As a result, some landslides may have been omitted. Moreover, only SAR phase information was used to detect and map active landslides, which is only suitable for slow-moving landslides. Therefore, some fast-moving landslides, such as those shown in Figs. 9a(3) and (18), are difficult to detect as a result of the large-gradient deformation.

5.2. Distribution pattern of the detected landslides with respect to topographic factors

Topographic metrics, including elevation and hillslope angle, are important factors in the formation and development of landslide hazards (Wu et al., 2018). Elevation is related to hillslope material, roads and river valleys, land cover, and the seismic wave amplification effect (Wu et al., 2018). In general, a slope with a larger slope angle is more susceptible to landslides, as there is greater sliding force on slopes with a significant gradient (Wu et al., 2018). The elevation map and slope angle were generated from the 30 m AW3D30 DSM, as shown in Fig. 11. Quantitative statistical analyses between the landslide distribution and elevation, the local relief with respect to the nearby Jinsha River, and

slope angle were also conducted, as shown in Fig. 12.

It can be seen from Figs. 11a and 12a that approximately 69% of the active landslides detected are distributed at elevations ranging from 1000 to 3000 m, which covers approximately 57% of the total study area. More active landslides occur below 3000 m than above (80.4% and 19.6%, respectively). In addition, it is apparent that the number of active landslides between 1000 and 2000 m increases with altitude while the number decreases with altitude at elevations above 2000 m. The maximum landslide density is located at elevations ranging from 1500 to 2000 m. Fig. 12b also indicates that most of the landslides detected (57%) were distributed in areas with an elevation difference of less than 900 m, and the densest landslide distribution occurred in areas with a relative elevation difference of 500 to 700 m. Moreover, the number of landslides decreases as the height difference increases when it is greater than 700 m, suggesting that the landslides are mainly distributed in areas close to Jinsha River.

The slope angle for the whole study area was divided into 12 categories: $< 10°$, $10–15°$, $15–20°$, $20–25°$, $25–30°$, $30–35°$, $35–40°$, $40–45°$, $45–50°$, $50–55°$, $55–60°$, and $> 60°$. We found that the study area is dominated by moderate to large slope angles (i.e., $10–45°$), covering approximately 83% of the total study area. The areas with slope angles of $15–20°$, $20–25°$, and $25–30°$ occupy approximately 13%, 14%, and 15% of the total study area, respectively. The landslide distribution map
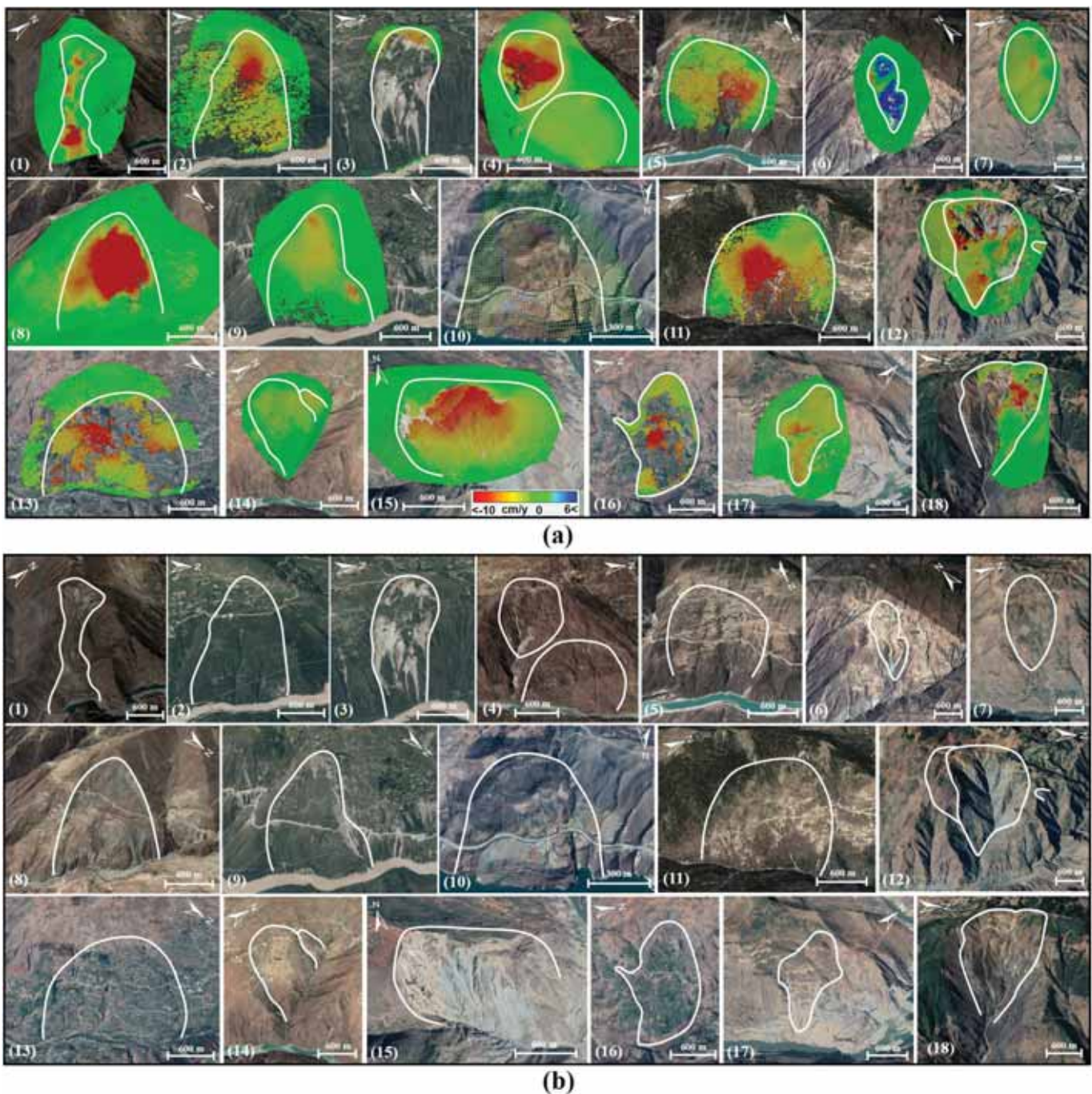
Fig. 9. (a) Enlarged deformation rate maps and (b) optical remote sensing images of 18 exemplary landslides. The white solid lines indicate the boundaries of the landslides. The optical remote sensing images were sourced from the Google Earth platform.

(Fig. 8) suggests that 74% of the active landslides detected are distributed in areas with slopes between 10° and 35°, while the maximum number of landslides is distributed where slopes are 15–25° (Figs. 11b and 12c). It can be seen from Fig. 12c that the number of landslides detected increases alongside the slope angle up to 15–20°, and then decreases as the slope angle increases further. Our observations are similar to the distributions of the landslides that were triggered by the Jiuzhaigou earthquake in southwest China in 2017 (Wu et al., 2018).

5.3. Causative factors of landslide activities

According to the results of the time series deformation, most of the landslides detected are deformed in a near linear trend, as shown in Figs. S7, S10, S11, and S12. However, some landslides exhibit obvious nonlinear deformation characteristics, particularly the landslides near Jinsha River (see Figs. S8 and S9). Two of the landslides labeled in Fig. 6 were selected as examples to investigate the causative factors of landslide activity over the Jinsha River corridor. The first, the Woda landslide, is located on the right bank of the Jinsha River near Woda village, Jiangda Country, Tibet (see Region B outlined with the white rectangle in Fig. 6 and No. 9 in Table 1). The Woda landslide is a huge ancient landslide, with a lateral width of 1080 m and a longitudinal length of 880 m. The second, the Xiaowanzi landslide, is located in the Xiluodu reservoir area (see Region U outlined with the white rectangle in Fig. 6).

Table 1
Summary of information for 69 landslides in the Jinsha River corridor characterized by high deformation rates.

No.	Landslide name	Length (m)	Width (m)	Slope angle (°)	Aspect (°)	Maximum LOS rate (mm/year)	SAR sensors	Time period (mm/yyyy- mm/yyyy)
1	Dangdi No.1	250	230	28–38	60	−104	S1	03/2017–11/2018
2	Dangdi No.2	214	396	26–44	16	−68	S1	03/2017–11/2018
3	Dangdi No.3	240	316	23–40	51	−77	S1	03/2017–11/2018
4	Ningkang	1900	609	10–42	118	−196	S1	03/2017–11/2018
5	Redangong	366	201	22–38	27	−50	S1	03/2017–11/2018
6	Aiguo	1101	1266	18–44	113	−162	S1	03/2017–11/2018
7	Aibai	1034	211	20–39	92	−60	S1	03/2017–11/2018
8	Gaina	1162	1024	16–39	30	−113	S1	03/2017–11/2018
9	Woda	880	1080	16–40	19	−115	S1	03/2017–11/2018
10	Moga	977	756	27–42	117	−36	S1, A2	10/2014–11/2018
11	Tange	1367	1096	22–45	67	−162	S1, A2	10/2014–11/2018
12	Duolai	825	373	18–36	108	−41	S1, A2	10/2014–11/2018
13	Shadingmai	1656	746	15–40	117	−95	S1, A2	10/2014–11/2018
14	Adong	908	440	19–39	51	−34	S1, A2	10/2014–11/2018
15	Xiaomojiu	1329	959	21–42	50	−61	S1, A2	10/2014–11/2018
16	Xiongba No.1	2586	2533	15–46	23	−97	S1	10/2014–11/2018
17	Xiongba No.2	2030	2027	15–51	133	−101	S1	10/2014–11/2018
18	Xiongba No.3	1359	1836	20–40	215	−31	S1	10/2014–11/2018
19	Semai	3069	1485	10–40	273	−71	S1	10/2014–11/2018
20	Wadui	2828	1196	16–40	107	−43	S1	10/2014–11/2018
21	Gongba	2395	982	15–39	112	−197	S1	10/2014–11/2018
22	Maiba No.1	719	372	24–42	243	−108	S1	10/2014–11/2018
23	Maiba No.2	359	256	34–46	222	−51	S1	10/2014–11/2018
24	Shangquesuo	2416	583	18–37	131	−50	S1	10/2014–11/2018
25	Shangde	992	464	16–37	28	−65	S1	10/2014–11/2018
26	Decun	1085	625	20–40	112	−56	S1	10/2014–11/2018
27	Suoxue	623	340	20–38	346	−67	S1	10/2014–11/2018
28	Chutigang No.1	656	291	19–44	162	−75	S1	10/2014–11/2018
29	Chutigang No.2	935	300	24–48	20	−57	S1	10/2014–11/2018
30	Caodigong	742	548	20–49	47	−122	S1	10/2014–11/2018
31	Suoduxi	390	378	11–30	124	−71	S1	10/2014–11/2018
32	Sarongxue	804	404	24–45	134	−36	S1	10/2014–11/2018
33	Nanagong	1242	493	10–40	44	−81	S1	10/2014–11/2018
34	Diwu	1511	727	10–30	217	120	S1	10/2014–11/2018
35	Namu	445	380	16–35	111	−37	S1	10/2014–11/2018
36	Linong	984	1329	15–64	95	−167	S1	10/2014–11/2018
37	Dagu	1000	470	18–56	142	−79	S1	10/2014–11/2018
38	Qinbei	625	459	10–16	107	−69	A2	09/2014–01/2019
39	Dongan No.1	690	515	10–33	12	−85	A2	09/2014–01/2019
40	Dongan No.2	642	583	12–33	21	−74	A2	09/2014–01/2019
41	Hongguang	613	295	21–36	64	−42	A2	09/2014–01/2019
42	Fangjiapo	468	351	27–43	128	−36	A2	09/2014–01/2019
43	Nawudu	682	860	16–45	11	−72	A2	09/2014–01/2019
44	Shangyingwo	938	496	16–51	113	−94	A2	09/2014–01/2019
45	Yazishou	745	392	15–36	190	−28	A2	09/2014–01/2019
46	Xincun	622	348	15–45	25	−41	A2	11/2014–03/2019
47	Zhongwushan	1791	889	10–55	78	−60	A2	09/2014–01/2019
48	Xiaoshuijing	648	421	24–44	185	−35	A2	09/2014–01/2019
49	Jinpingzi	2062	1116	10–40	141	−74	A2	09/2014–01/2019
50	Dadi	1007	1359	10–51	171	−102	A2	09/2014–01/2019
51	Yangpengzi	460	317	34–51	144	−52	A2	09/2014–01/2019
52	Luogazhi	1116	747	13–47	104	−84	A2	09/2014–01/2019
53	Yeniuping	611	659	29–45	178	−45	A2	09/2014–01/2019
54	Hejialiangzi	908	245	14–30	230	80	A2	09/2014–01/2019
55	Damuchun	463	573	14–40	209	−89	A2	09/2014–01/2019
56	Dashannao	775	1745	17–51	178	−34	A2	10/2014–03/2019
57	Yezhutang	842	460	11–41	61	−62	A2	10/2014–03/2019
58	Huangtian	441	372	13–28	62	−51	A2	10/2014–03/2019
59	Jiashantian	573	352	14–34	121	−43	A2	10/2014–03/2019
60	Zengjiawanzi	1051	578	14–46	308	−56	A2	01/2015–11/2016
61	Yizi	939	265	10–22	290	−63	A2	01/2015–11/2016
62	Ximaxi	1497	1139	10–50	98	−87	A2	01/2015–11/2016
63	Yanwan	863	657	20–42	77	−70	A2	01/2015–11/2016
64	Ribucu	576	598	29–42	25	−56	A2	01/2015–11/2016
65	Shangshawa	661	903	10–38	145	−50	A2	09/2014–12/2018
66	Nongle	1358	1415	10–60	106	−108	A2	09/2014–12/2018
67	Xianglushan	416	652	13–31	150	−75	A2	09/2014–12/2018
68	Wufutang	1015	685	10–30	40	−139	A2	09/2014–12/2018
69	Guanghui	535	589	10–23	216	70	A2	10/2014–11/2018

Note that the length and width of the landslides were measured based on the InSAR-derived deformation area, the landslides were named after the geographic name of an area, and the slope angle and aspect were calculated using DEM. S1 and A2 represent Sentinel-1 and ALOS/PALSAR-2 SAR images, respectively.
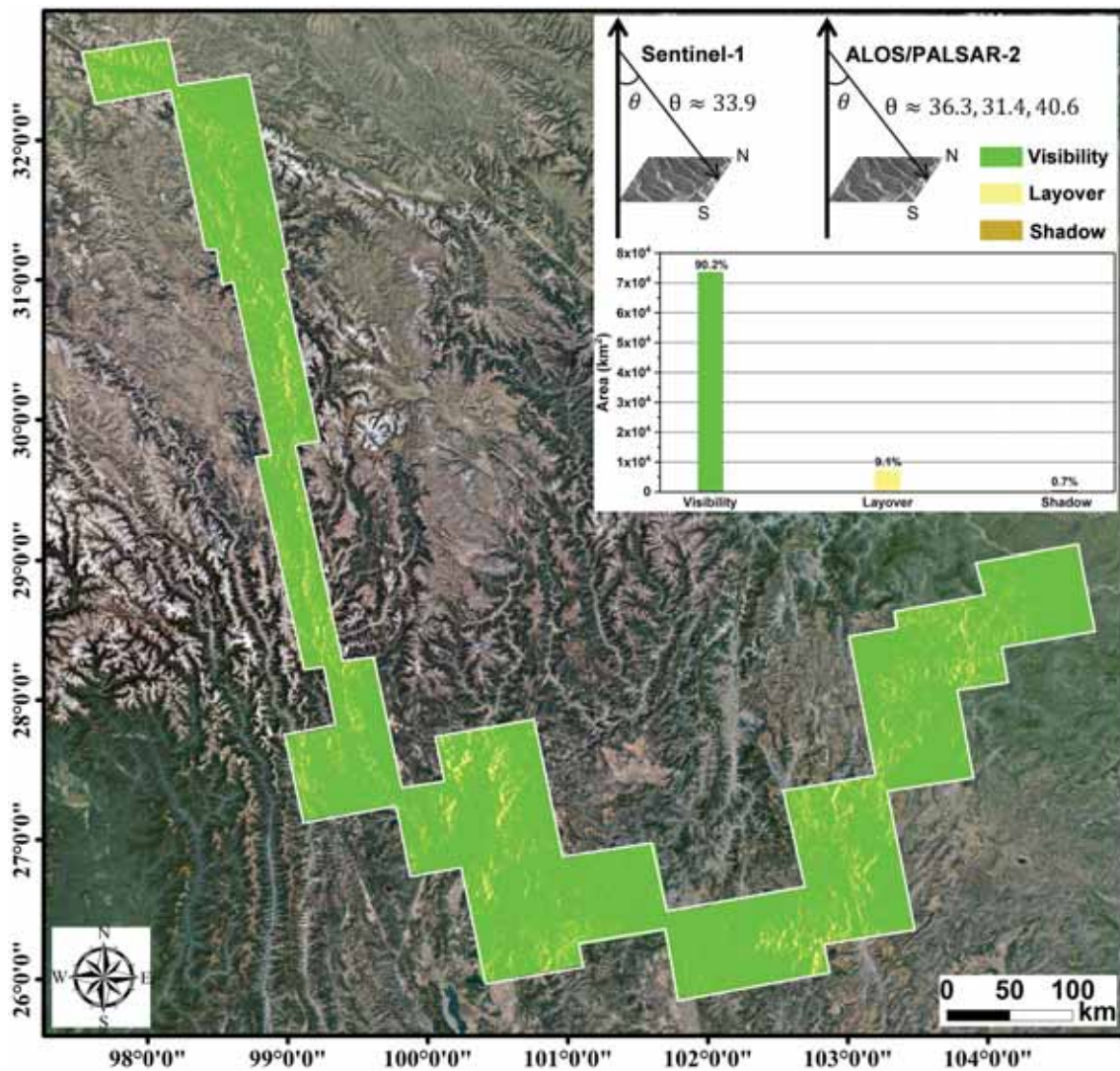
Fig. 10. Geometrical distortions (layover and shadow) and visibility of the ascending Sentinel-1 and ALOS/PALSAR-2 SAR images over the Jinsha River corridor.

This landslide has a relatively small size, at approximately only 260 m in width and 320 m in length. Evidence from optical remote sensing images shows that the toe of the landslide intersects the Jinsha River.

Fig. 13a shows the annual deformation rate of the Woda landslide calculated using the Sentinel-1 images for the period from March 18, 2017 to November 20, 2018, and Figs. 13b and c show the time series deformation of Points P13 and P14 (marked by the white rhombuses in Fig. 13a) against monthly precipitation. As shown in Fig. 13a, strong areas of deformation were detected in the trailing edge and the middle of the landslide, and the maximum deformation rate was approximately −115 mm/year. As shown in Figs. 13b and c, the landslide deformation is closely correlated with monthly precipitation, and a significant acceleration in the deformation resulting from heavy rainfall during the rainy season is clear. The landslide was in a stable state before July 2017, when reactivation and significant acceleration in deformation occurred as a result of successive heavy rainfall. The deformation decreased during the period from November 2017 to June 2018 as a result of the decrease in precipitation. However, the deformation accelerated once again when intensive rainfall of more than 190 mm occurred in July 2018. This evidence suggests that heavy rainfall during the summer is a significant factor of landslide activity over the Jinsha River corridor.

Fig. 14a shows the annual deformation rate of the Xiaowanzi landslide from September 21, 2014 to July 9, 2017 calculated using the

ALOS/PALSAR-2 images, and Figs. 14b and c are time series deformations of Points P15 and P16 (marked by the white rhombuses in Fig. 14a) versus variations in the water level of Jinsha River in the Xiluodu reservoir area, which has experienced three high-water impoundments during which the water level fluctuated between 540 and 600 m since May 2013. Many new landslides were triggered and ancient landslides were reactivated during this period (Chen and Dai, 2018). Figs. 14 b and c indicate that the Jinsha River water level at the Xiluodu reservoir underwent three annual rise–decline cycles corresponding to impoundment–discharge operations at the reservoir. The water level increased from to 546 m on June 21, 2015 to 599 m on October 22, 2015 and decreased again to 547 m on May 26, 2016. As shown in Figs. 14b and c, the deformation of the landslide accelerated significantly during the rapid decline of the water level, and the deformation rate of the landslide is positively correlated with the rate at which the water level declines. The landslide deformation accelerated again with a rapid decline in the water level between October 25, 2016 and June 27, 2017. The evidence therefore indicates that a rapid decline in the water level of Jinsha River is also a significant factor of landslide activity.

6. Conclusions

The Jinsha River corridor, with its extensive distribution and strong activity of landslide hazards, requires to early identify and closely
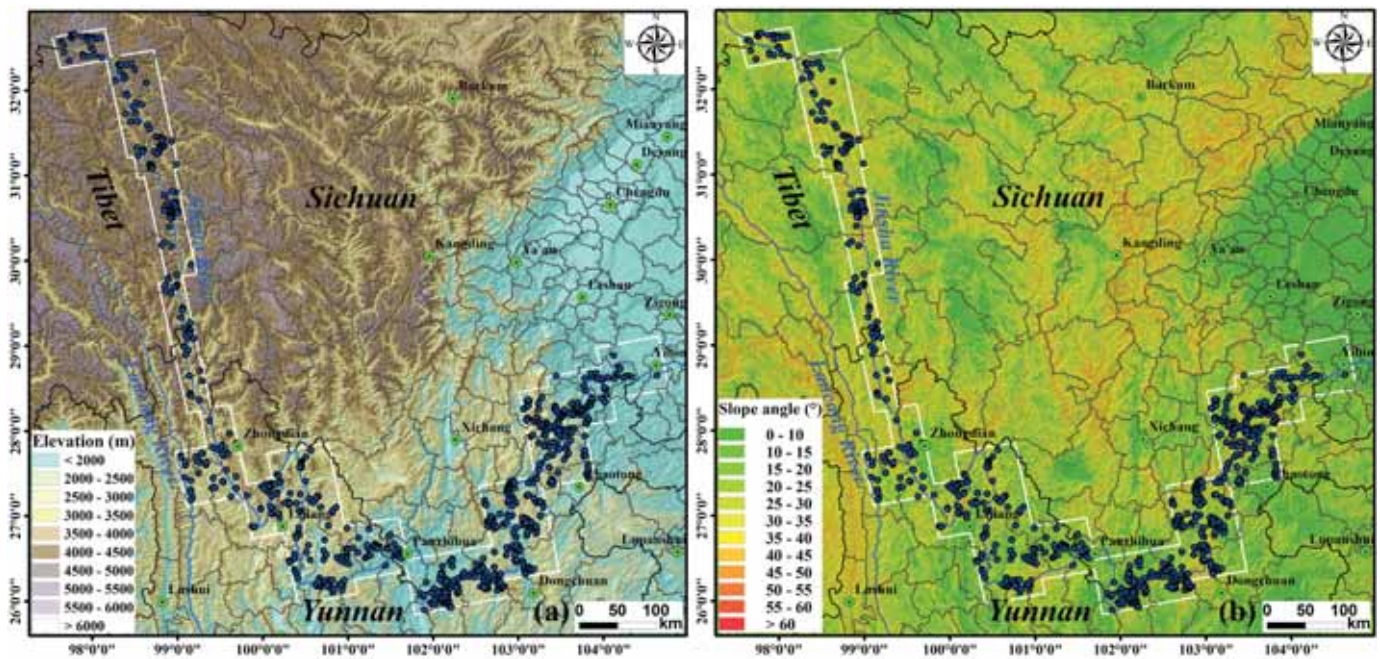
Fig. 11. Spatial distribution of detected active landslides along the Jinsha River corridor on maps of (a) elevation and (b) slope angle.
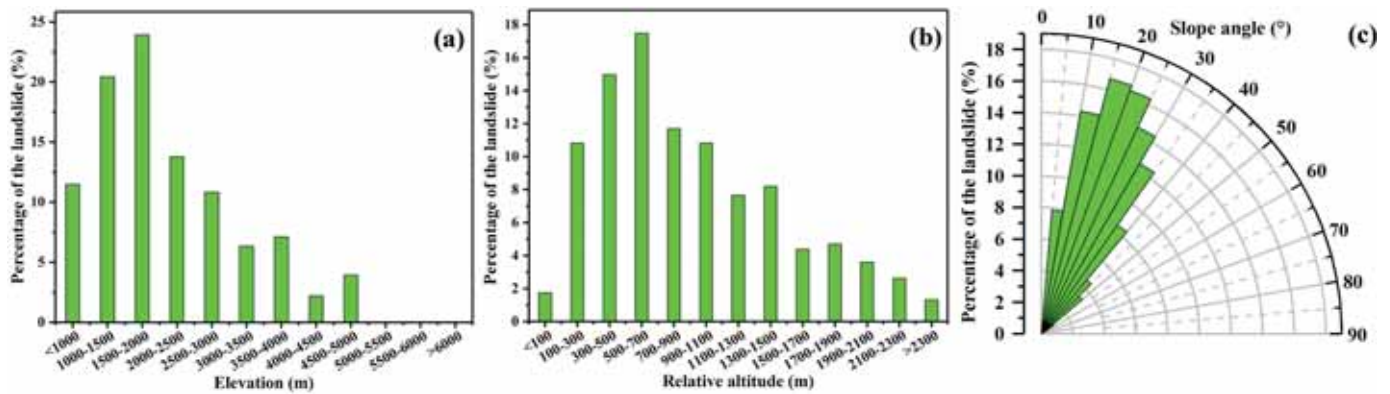

Fig. 12. Statistics of landslide distribution versus elevation (a); local relief with respect to the nearby Jinsha River (b); and slope angle (c).

monitor the potential hazards. We developed a new InSAR-based procedure for large-area active landslide mapping in geomorphologically complex areas by combining surface deformation features with geomorphological features. We generated a comprehensive distribution map of the active landslides along the Jinsha River corridor through the integration of Sentinel-1 and ALOS/PALSAR-2 SAR images based on the proposed procedure. A total of 915 active landslides were detected and mapped over an area of approximately 81,667.6 km², of which 69 landslides were in close vicinity to Jinsha River. These landslides pose a risk of blocking the river, threatening the safety of hydropower stations if a failure occurs; the situation therefore demands widespread attention and should be monitored by in situ facilities such as GNSS. We came to the conclusion that InSAR measurements can play a significant role in the detection of active landslides and the accurate delineation of the boundaries of slope activity in the Jinsha River corridor. Furthermore, the proposed method is of greatly applicable significance for detecting and mapping landslides in geomorphologically complex areas.

The active landslides detected were unevenly distributed along the Jinsha River corridor and were concentrated mainly around the Wudongde, Baihetan, and Xiluodu reservoirs. Six regions including many large-scale landslides (with a length and/or width of >1 km) were

found. The landslides were mainly concentrated in areas with elevation ranging from 1500 to 2000 m and slope angles of 15–25°. Time series analyses of the deformation demonstrates that heavy rainfall in the summer and the rapid decline of the water level in the Jinsha River are among significant factors of landslide activity. The rate at which the slope moves is positively correlated with the rate of decline in the water level. Real-time monitoring of landslide deformation, rainfall, and the water level of the Jinsha River is therefore essential for the prevention and early warning of landslide hazards. These findings provide a significant reference for the management and mitigation of landslide disaster chains over the Jinsha River corridor.

In this study, the SAR images of some areas were affected by geometrical distortion due to the steep terrain, meaning that landslides occurring in these areas may have been omitted. The combination of SAR images from ascending and descending orbits may solve this problem to a certain extent in the future. On the other hand, decorrelation caused by extremely dense vegetation and large-gradient landslide deformation is inevitable, severely limiting the application of phase-based InSAR techniques for large-area landslide detection and may lead to landslide omission. The latter problem is expected when using amplitude-based offset-tracking method. Moreover, based on
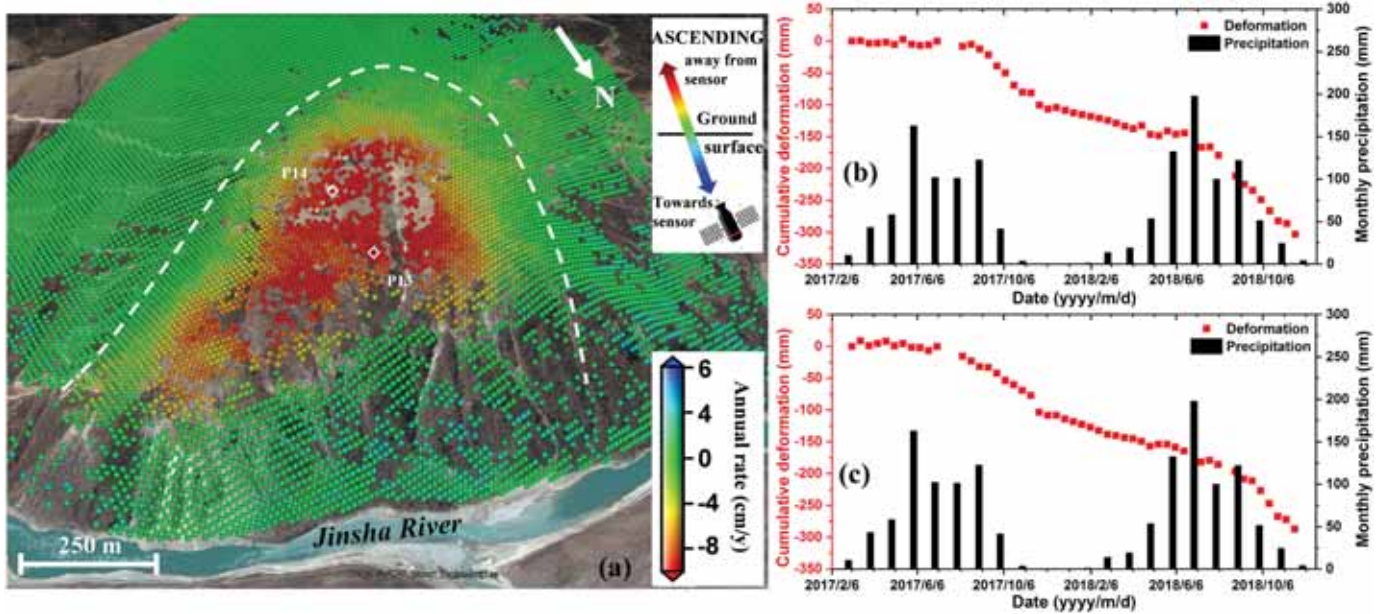
Fig. 13. Relationship between slope deformation and precipitation for the Woda landslide. (a) Annual deformation rate from March 18, 2017 to November 20, 2018; (b) time series deformation of Point P13 against monthly precipitation; and (c) time series deformation of Point P14 against monthly precipitation.
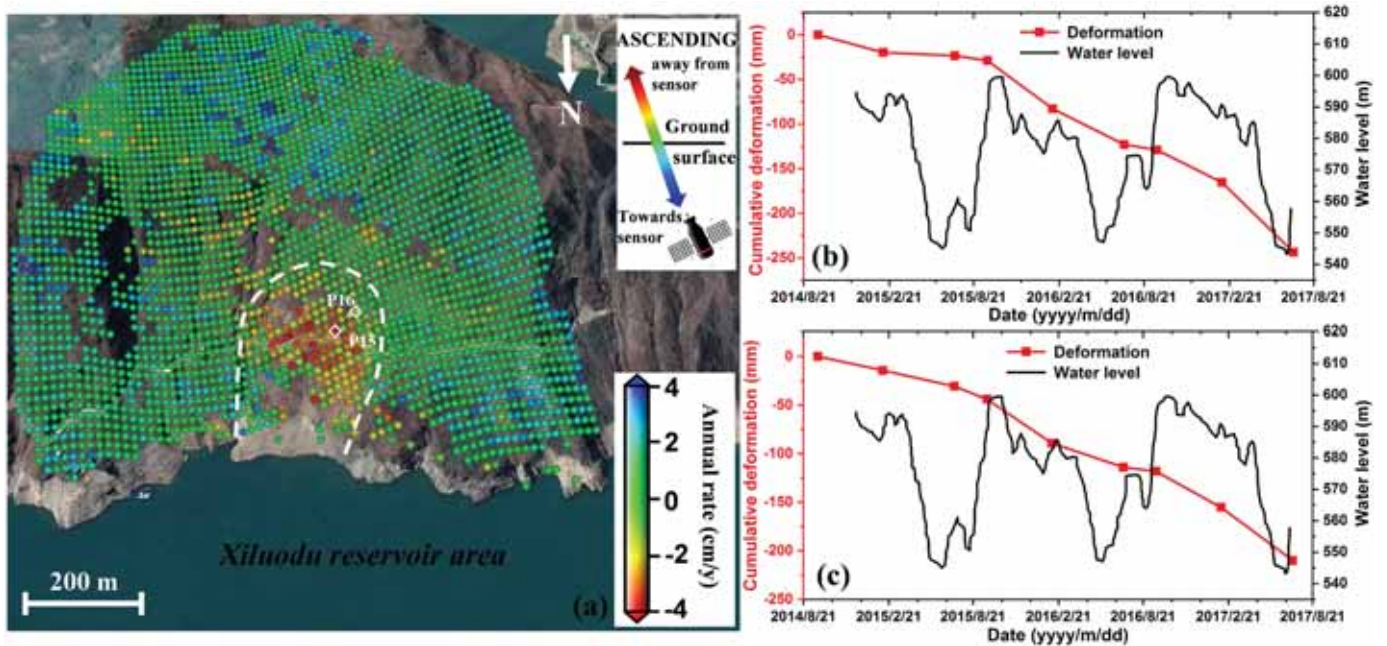

Fig. 14. Relationship between slope deformation and variations in the water level of Jinsha River at the Xiaowanzi landslide. (a) Annual deformation rate between September 21, 2014 and July 9, 2017; (b) time series deformation of Point P15 versus variations in the water level of Jinsha River at the Xiluodu reservoir; and (c) time series deformation of Point 16 versus variations in the water level of Jinsha River at the Xiluodu reservoir.

landslide inventory mapping results, it is important to investigate the types and failure modes of landslides for early warning of hazards by combining hydrological factors with ground-based real-time deformation measurements.

Author statement

All persons who have made substantial contributions to the work reported in the manuscript, and reviewed and approved the manuscript. Xiaojie Liu and Chaoying Zhao proposed the methodology. Xiaojie Liu and Liquan Chen performed the experiments and produced the results.

Xiaojie Liu drafted the manuscript and Chaoying Zhao finalized the manuscript. Qin Zhang, Zhong Lu, Zhenhong Li, Chengsheng Yang, Wuzhu and Jing Liu-Zeng contributed to the analysis and discussion of the results. Zhong Lu, Zhenhong Li and Jing Liu-Zeng provided writing and editing assistance. Chuanjin Liu provided historical earthquake data and helped the analysis of the results.

All funds supporting this research were acknowledged in the Acknowledgements section, and all data involved in this study were also acknowledged.

In addition, we thank very much for the constructive and insightful comments from the editor and two anonymous reviewers. We have

made substantial revisions based on all comments and suggestions.

Declaration of Competing Interest

The authors declare no conflict of interest.

Appendix A. Supplementary data

Supplementary data to this article can be found online at https://doi.org/10.1016/j.enggeo.2021.106033.

References

Behling, R., Roessner, S., Golovko, D., Kleinschmit, B., 2016. Derivation of long-term spatiotemporal landslide activity- a multi-sensor time series approach. Remote Sens. Environ. 186, 88–104.

Berardino, P., Fornaro, G., Lanari, R., Sansosti, E., 2002. A new algorithm for surface deformation monitoring based on small baseline differential SAR interferograms. IEEE Trans. Geosci. Remote Sens. 40 (11), 2375–2383.

Chen, T.Z., Dai, F.C., 2018. Exploring the landslide deformation regular based after the impoundment in the Xiluodu reservoir. Indust. Construct. 48, 634–639 (In Chinese).

Costantini, M., 1998. A novel phase unwrapping method based on network programming. IEEE Trans. Geosci. Remote Sens. 36, 813–821.

Doin, M.P., Lasserre, C., Peltzer, G., Cavalié, O., Doubre, C., 2009. Corrections of stratified tropospheric delays in SAR interferometry: validation with global atmospheric models. J. Appl. Geophys. 69 (1), 35–50.

Dong, J., Liao, M.S., Xu, Q., Zhang, L., Tang, M.G., Gong, J.Y., 2018. Detection and displacement characterization of landslides using multitemporal satellite SAR interferometry: a case study of Danba County in the Dadu River Basin. Eng. Geol. 240, 95–109.

Du, J., Glade, T., Woldai, T., Chai, B., Zeng, B., 2020. Landslide susceptibility assessment based on an incomplete landslide inventory in the Jilong Valley, Tibet, Chinese Himalayas. Eng. Geol. 270, 105572.

Goldstein, R.M., Werner, C.L., 1998. Radar interferogram filtering for geophysical applications. Geophys. Res. Lett. 25, 4035–4038.

Harp, E.L., Keefer, D.K., Sato, H.P., Yagi, H., 2011. Landslide inventories: the essential part of seismic landslide hazard analyses. Eng. Geol. 122, 9–21.

Hu, G.S., Tian, S.F., Chen, N.S., Liu, M., 2020. An effectiveness evaluation method for debris flow control engineering for cascading hydropower stations along the Jinsha River, China. Eng. Geol. 266, 105472.

Huffman, G.J., Stocker, E.F., Bolvin, D.T., Nelkin, E.J., Tan, J., 2019. GPM IMERG final precipitation L3 month 0.1 degree × 0.1 degree V06, Greenbelt, MD. Goddard Earth Sciences data and Information Services Center (GES DISC), Accessed: [26 July 2019]. https://doi.org/10.5067/GPM/IMERG/3B-MONTH/06.

Iqbal, J., Dai, F.C., Hong, M., Tu, X.B., Xie, Q.Z., 2018. Failure mechanism and stability analysis of an active landslide in the Xiangjiaba reservoir area, Southwest China. J. Earth Sci. 29, 646–661.

Kang, Y., Zhao, C.Y., Zhang, Q., Lu, Z., Li, B., 2017. Application of InSAR techniques to an analysis of the Guanling landslides. Remote Sens. 9, 1046.

Li, Y., Fan, X.Y., Cheng, G.W., 2006. Landslide and rockfall distribution by reservoir of stepped hydropower station in the Jinsha River. Wuhan Univ. J. Nat. Sci. 4, 801–805.

Li, L.J., Yao, X., Yao, J.M., Zhou, Z.K., Feng, X., Liu, X.H., 2019. Analysis of deformation characteristics for a reservoir landslide before and after impoundment by multiple D-InSAR observations at Jinshajiang River, China. Nat. Hazards 98, 719–733.

Liang, G.L., Wang, Z., Zhang, G.W., Wu, L.L., 2019. Two huge landslides that took place in quick succession within a month at the same location of Jinsha River. Landslides 16, 1059–1062.

Liu, H.J., Lan, H.X., Liu, Y., Zhou, Y., 2011. Characteristics of spatial distribution of debris flow and the effect of their sediment yield in main downstream of Jinsha River. China. Environ. Earth Sci. 64, 1653–1666.

Liu, X.J., Zhao, C.Y., Zhang, Q., Peng, J.B., Zhu, W., Lu, Z., 2018. Multi-temporal loess landslide inventory mapping with C-, X- and L-Band SAR datasets—a case study of Heifangtai loess landslides, China. Remote Sens. 10, 1756.

Liu, X.J., Zhao, C.Y., Zhang, Q., Yang, C.S., Zhang, J., 2019. Characterizing and monitoring ground settlement of marine reclamation Land of Xiamen New Airport, China with Sentinel-1 SAR Datasets. Remote Sens. 11, 585.

Liu, X.J., Zhao, C.Y., Zhang, Q., Lu, Z., Li, Z.H., 2020. Deformation of the Baige Landslide, Tibet, China, revealed through the integration of cross-platform ALOS/PALSAR-1 and ALOS/PALSAR-2 SAR observations. Geophys. Res. Lett. 47, 1–8.

Lyons, S., Sandwell, D., 2003. Fault creep along the southern San Andreas from interferometric synthetic aperture radar, permanent scatterers, and stacking. J. Geophys. Res. Solid Earth 108.

Nishiguchi, T., Tsuchiya, S., Imaizumi, F., 2017. Detection and accuracy of landslide movement by InSAR analysis using PALSAR-2 data. Landslides 1–8.

Rosi, A., Tofani, V., Tanteri, L., Tacconi Stefanelli, C., Agostini, A., Catani, F., Casagli, N., 2018. The new landslide inventory of Tuscany (Italy) updated with PS-InSAR: geomorphological features and landslide distribution. Landslides 15, 5–19.

Scaioni, M., Longoni, L., Melillo, V., Papini, M., 2014. Remote Sensing for landslide investigations: an overview of recent achievements and perspectives. Remote Sens. 6, 1–53.

Shi, X.G., Liao, M.S., Li, M.H., Zhang, L., Cunningham, C., 2016. Wide-area landslide deformation mapping with multi-path ALOS/PALSAR data stacks: a case study of three Gorges area, China. Remote Sens. 8, 136.

Shi, X.G., Yang, C., Zhang, L., Jiang, H.J., Liao, M.S., Zhang, L., Liu, X.J., 2019. Mapping and characterizing displacements of active loess slopes along the upstream Yellow River with multi-temporal InSAR datasets. Sci. Total Environ. 674, 200–210.

Song, D.Q., Che, A.L., Chen, Z., Ge, X.R., 2018. Seismic stability of a rock slope with discontinuities under rapid water drawdown and earthquakes in large-scale shaking table tests. Eng. Geol. 245, 153–168.

Veci, L., Lu, J., Prats-Iraola, P., Scheiber, R., Collard, F., Fomferra, N., Engdahl, M., 2014. The Sentinel-1 Toolbox. In Proceeding of the IEEE International Geoscience and Remote Sensing Symposium (IGASS), Quebec City, Canada, 13–18 July 2014; pp. 1–3.

Wang, G.J., Xie, M.W., Chai, X.Q., Wang, L.W., Dong, C.X., 2013. D-InSAR-based landslide location and monitoring at Wudongde hydropower reservoir in China. Environ. Earth Sci. 69, 2763–2777.

Wasowski, J., Bovenga, F., 2014. Investigating landslides and unstable slopes with satellite Multi Temporal Interferometry: current issues and future perspectives. Eng. Geol. 174, 103–138.

Wasowski, J., Bovenga, F., 2015. Remote sensing of landslide motion with emphasis on satellite multitemporal interferometry applications: an overview. In: Davies, T. (Ed.), Landslide Hazards, Risks and Disasters, pp. 345–403.

Wu, C.H., Cui, P., Li, Y.S., Irasema, A.A., Huang, C., Yi, S.J., 2018. Seismogenic fault and topography control on the spatial patterns of landslides triggered by the 2017 Jiuzhaigou earthquake. J. Mt. Sci. 15, 793–807.

Xu, W.Y., Zhang, Q., Zhang, J.C., Wang, R.B., Wang, R.K., 2013. Deformation and control engineering related to huge landslide on left bank of Xiluodu reservoir, south-West China. Eur. J. Environ. Civ. Eng. 17, 249–268.

Yu, C., Li, Z.H., Penna, N.T., 2018a. Interferometric synthetic aperture radar atmospheric correction using a GPS-based iterative tropospheric decomposition model. Remote Sens. Environ. 204, 109–121.

Yu, C., Li, Z., Penna, N.T., Crippa, P., 2018b. Generic atmospheric correction model for Interferometric Synthetic Aperture Radar observations. J. Geophys. Res. Solid Earth 123, 9202–9222.

Yu, J.S., Tan, K., Zhang, C.H., Zhao, B., Wang, D.Z., Li, Q., 2019. Present-day crustal movement of the Chinese mainland based on Global Navigation Satellite System data from 1998 to 2018. Adv. Space Res. 63, 840–856.

Zhang, Y.S., Zhao, X.T., Lan, H.X., Xiong, T.Y., 2011. A Pleistocene landslide-dammed lake, Jinsha River, China. Quat. Int. 233, 72–80.

Zhang, Y., Meng, X.M., Chen, G., Qiao, L., Zeng, R.Q., Chang, J., 2015. Detection of geohazards in the Bailongjiang River basin using synthetic aperture radar interferometry. Landslide 13, 1273–1284.

Zhao, C.Y., Lu, Z., Zhang, Q., Fuente, J.D.L., 2012. Large-area landslide detection and monitoring with ALOS/PALSAR imagery data over Northern California and Southern Oregon, USA. Remote Sens. Environ. 124, 348–359.

Zhao, C.Y., Kang, Y., Zhang, Q., Lu, Z., Li, B., 2018. Landslide Identification and monitoring along the Jinsha River Catchment (Wudongde Reservoir Area), China, using the InSAR Method. Remote Sens. 10, 993.

Zhou, J.W., Xu, W.Y., Yang, X.G., Shi, C., Wang, Z.H., 2010. The 28 October 1996 landslide and analysis of the stability of the current Huashiban slope at the Liangjiaren Hydropower Station, Southwest China. Eng. Geol. 114, 45–56.

Zhou, C., Yin, K.L., Cao, Y., Intrieri, E., Ahmed, B., Catani, F., 2018. Displacement prediction of step-like landslide by applying a novel kernel extreme learning machine method. Landslides 2211–2225.

Zhuang, J.Q., Peng, J.B., Wang, G.H., Javed, J., Wang, Y., Li, W., 2018. Distribution and characteristics of landslide in Loess Plateau: a case study in Shaanxi province. Eng. Geol. 236, 89–96.